International Journal of Heat and Mass Transfer 122 (2018) 939–953

Contents lists available at ScienceDirect

International Journal of Heat and Mass Transfer

journal homepage: www.elsevier.com/locate/ijhmt

Use of a mixed columnar-equiaxed solidification model to analyse the formation of as-cast structure and macrosegregation in a Sn-10 wt% Pb benchmark experiment

Y Zheng [a], M Wu [a,b,*], E Karimi-Sibaki [a,b], A Kharicha [a,b], A Ludwig [a]

[a] Chair of Modelling and Simulation of Metallurgical Processes, Montanuniversitaet Leoben, Austria
[b] Christian Doppler Laboratory for Advanced Simulation of Solidification and Melting, Montanuniversitaet Leoben, Austria

ARTICLE INFO

Article history:
Received 28 November 2017
Received in revised form 22 January 2018
Accepted 5 February 2018

Keywords:
Macrosegregation
As-cast structure
Fragmentation
Crystal sedimentation
Columnar-to-equiaxed transition (CET)
Channel segregation

ABSTRACT

A solidification benchmark experiment based on a Sn-10 wt% Pb alloy was performed at the SIMAP Laboratory in Grenoble, France, to investigate the formation of as-cast structure and macro- and mesosegregation (Wang et al., 2009; Hachani et al., 2015). The current study simulated this benchmark using a mixed columnar-equiaxed solidification model. This model was developed by the current authors (Wu et al., 2006), and recently extended to consider the crystal fragmentation of columnar dendrites as the source of equiaxed grains. A satisfactory experiment-simulation agreement in the temperature evolution, the as-cast structure, and the distribution of macro- and mesosegregation, was obtained. By analysis of the modelling results, new knowledge regarding the formation of the as-cast structure (mixed columnar-equiaxed) was obtained: The fragmentation-induced equiaxed crystals are transported away from the front region of the columnar zone by the melt flow; those crystals continue to grow or re-melt depending on the condition of local constitutional undercooling or supersaturation; the density of the melt varies with the Pb enrichment in the melt, and the equiaxed crystals can settle down or float up through the balance of the flow-induced drag force and the gravity-driven sedimentation; it is the motion of equiaxed crystals that determines the final distribution of the equiaxed zone in this benchmark experiment; the interdendritic flow and its interaction with the solidification in the front region of the columnar zone lead to the formation of segregation channels.

1. Introduction

Laboratory solidification experiments with Pb-Sn and Pb-Zn alloys, following the configuration of Hebditch and Hunt [1], were widely used to investigate the formation of as-cast structure and macrosegregation [2–4]. Recently, a sophisticated AFRODITE setup with precise control of cooling rate and temperature gradient was designed, and a series of solidification experiments and post-mortem metallographic and compositional analyses of as-solidified samples were performed at the SIMAP Laboratory in Grenoble, France [5–8]. Fig. 1 shows the configuration of the AFRODITE setup. Hachani et al. [7] presented comprehensive results regarding the temperature measurement, as-cast structure, and macro- and mesosegregation. Sn-10 wt% Pb alloy was considered. The current study simulated this benchmark using a mixed columnar-equiaxed solidification model, as developed by the authors [9]. In the original experiments of Hachani et al. [7], both solidification experiments under forced convection (with electromagnetic stirring) and under natural convection (gravity only) were performed. In the current study, however, only the experiment under natural convection was numerically investigated.

Previously, simulation studies with different numerical methods were reported for these benchmark experiments [6,10–12]. The cellular automaton and finite element method (CAFE) was successfully used to simulate the equiaxed distribution and the global macrosegregation [10,11]. The drawback of this stochastic method is that, in additional to the high computational cost due to the vast number of equiaxed crystals, the mesosegregation (segregation channels) and the equiaxed crystals as created by fragmentation have not been resolved. The multiphase volume or ensemble averaging technique was proposed to model the dendritic solidification of columnar or/and equiaxed structure [12–16]. By introducing a concept of grain envelope, the extra- and interdendritic melts, whose concentrations are significantly different, can be considered

* Corresponding author at: Chair of Modelling and Simulation of Metallurgical Processes, Montanuniversitaet Leoben, Austria.
E-mail address: menghuai.wu@unileoben.ac.at (M Wu).

https://doi.org/10.1016/j.ijheatmasstransfer.2018.02.012
0017-9310/

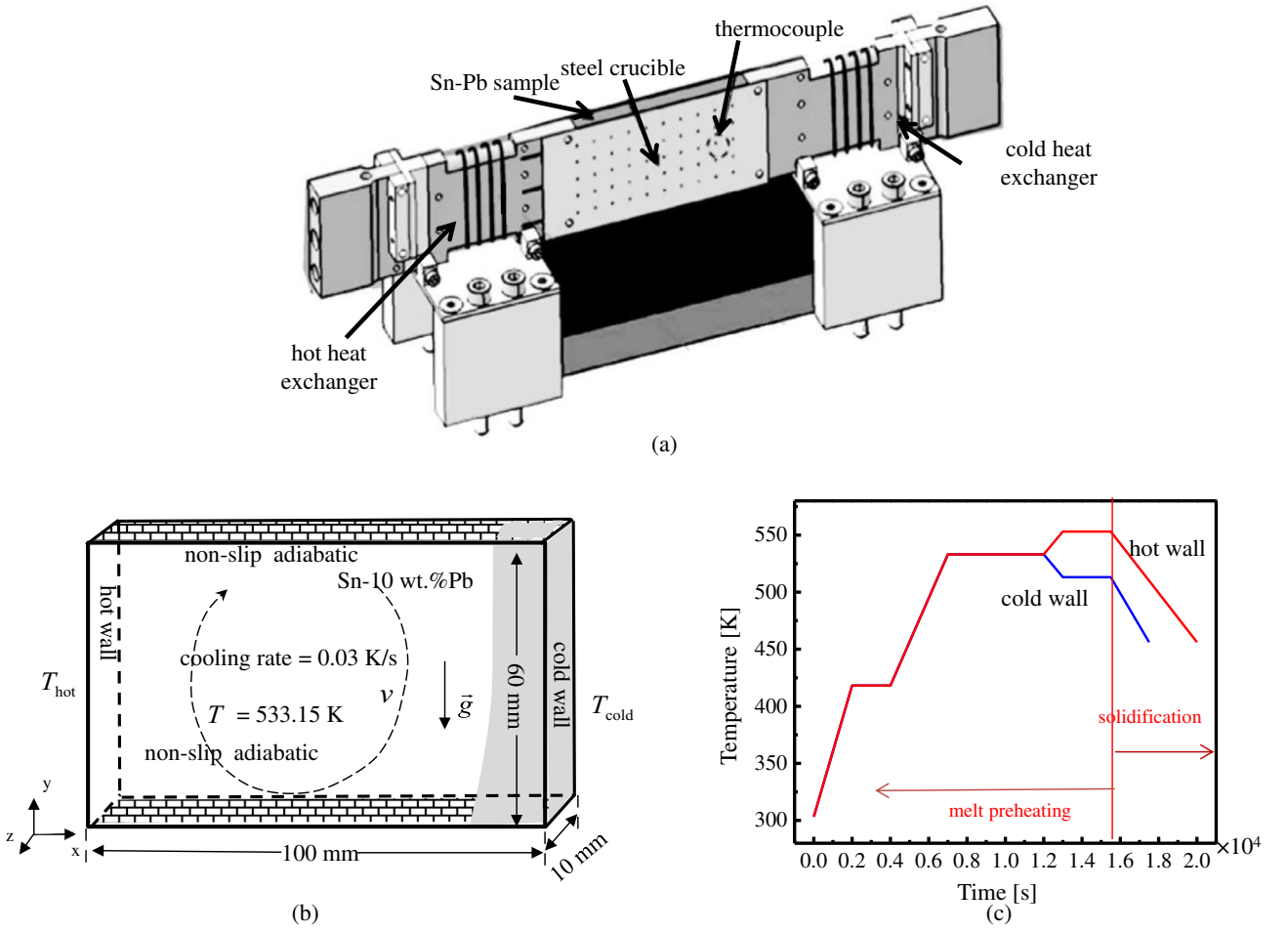

Fig. 1. Configuration of the AFRODITE setup [7]: (a) Schematic view of the experimental facility, (b) geometry and boundary conditions of the benchmark casting, and (c) temperature history experimentally applied at the boundaries of the hot and cold walls. (b) and (c) are reprinted from publication [7], with permission from Elsevier.

as different phases or phase regions. However, the more the phase regions, the larger the computation resource is demanded. To treat the mixed columnar-equiaxed solidification with dendritic morphology, five phase region are necessarily considered [14,15]. Therefore, some people used a mixture continuum solidification model [6,17] to calculate the macro- and mesosegregation. A drawback of the continuum solidification model is that it fails to distinguish the free-moving equiaxed crystals from the stationary columnar structure. A three-phase volume-average-based model was proposed by Wu et al. [9,18] to simulate the mixed columnar-equiaxed solidification. The tracking of the columnar tip front, the formation of equiaxed crystals based on the heterogeneous nucleation and the motion of equiaxed crystals, were considered.

This model has been satisfactorily applied to investigate the formation of as-cast structure (mixed columnar-equiaxed) and macrosegregation in steel and aluminium alloy ingots [19,20], and it was also applied to study the macrosegregation as observed in the Hebditch-Hunt benchmark experiments [21,22].

Unfortunately, the previous volume-average-based model has ignored the fragmentation phenomenon, which was believed to be the most important source of equiaxed crystals in the Sn-10 wt% Pb benchmark solidification experiment [7]. Therefore, the three-phase mixed columnar-equiaxed solidification model was recently extended by incorporating the crystal fragmentation of columnar dendrites as a source of equiaxed crystals [23]. It is this extended model that is used for the current study.

One goal of this work is to further validate the mixed columnar-equiaxed solidification model by 'reproducing' the benchmark experiment. The ultimate goal is to explain the formation of the special pattern of as-cast structure and the macro- and mesosegregation. According to Hachani et al. [7], no comprehensive explanation to them has yet been achieved.

2. Model description

A three-phase mixed columnar-equiaxed solidification model [9] was adopted. The key features and assumptions are:

(1) The three phases are the primary melt, equiaxed, and columnar phases. Their volume fractions are quantified by f_ℓ, f_e and f_c, and $f_\ell + f_e + f_c = 1$. Both the liquid and equiaxed phases are moving phases, and the corresponding Navier-Stokes equations are solved. The columnar phase is assumed to be rigid and stationary.

(2) Columnar trunks (morphology) are approximated by stepwise cylinders, originating from the mould wall. Equiaxed crystals originate from fragmentation (see further description herein). To calculate the growth of equiaxed grains, a globular (spherical) morphology is assumed. However, to calculate the drag force and other hydrodynamic interactions, a simplified dendritic morphology of equiaxed crystal is considered. This simplified dendritic morphology is described by an equiaxed grain envelope, which includes

the solid 'dendrite' and the inter-dendritic melt. The volume ratio of the solid 'dendrite' to the equiaxed grain envelope is predefined: f_{si}. In this study, f_{si} is set as a constant value (0.5).

(3) When the volume fraction of the equiaxed grain envelope ($f_e^{Env} = f_e/f_{si}$) reaches the blocking criterion $f_{e,CET}$ (=0.49) at the columnar tip front, the columnar-to-equiaxed transition (CET) occurs [24]. In the opposite scenario, the columnar phase can also grow from the packed equiaxed zone, and equiaxed-to-columnar transition (ECT) occurs [25].

(4) The interactions between neighbouring equiaxed crystals and their influence on the motion of the equiaxed phase is modelled by a so-called effective viscosity (μ_e) [26], which increases with the volume fraction of the equiaxed phase. When the volume fraction of the equiaxed phase grain envelope f_e^{Env} reaches the packing limit $f_{e,packing}$ (=0.637), μ_e increases to infinity, and a rigid network of equiaxed crystals is built.

(5) The presence of the columnar structure influences the motion of equiaxed crystals. The equiaxed crystals can be captured by the columnar dendrite trunk when the local volume fraction of the columnar phase reaches a critical value of $f_c^{free} = 0.2$.

(6) Resistance of the mushy zone (columnar phase) to interdendritic flow is calculated using a permeability law according to Blake-Kozeny [27]. The drag force coefficient $K_{\ell c}$ for the liquid-equiaxed interaction is treated according to Kozeny-Carman for $f_e^{Env} < 0.7$, and Blake-Kozeny for $f_e^{Env} \geqslant 0.7$ [27].

(7) The solidification of the columnar phase competes with that of the equiaxed crystals. The solidification of both columnar trunk and equiaxed crystals is governed by diffusion; the difference between equilibrium and volume-averaged melt concentrations ($c_\ell^* - c_\ell$) is the driving force for the solidification. If the driving force ($c_\ell^* - c_\ell$) < 0, remelting would occur.

(8) In this study, fragmentation of columnar dendrites is considered as the only source of equiaxed crystals. Following the consideration that solute-driven remelting of secondary or high-order dendrites is the key mechanism for fragmentation [27–32], a new formula was proposed for the fragmentation-induced mass transfer rate [23]: $M_{ce} = -\gamma \cdot \vec{u}_\ell \cdot \nabla c_\ell \cdot \rho_e$. This means that an interdendritic flow in the columnar zone $\vec{u}_\ell$ against the direction of the melt concentration gradient ($-\nabla c_\ell$) increases the local constitutional supersaturation, hence promoting remelting-induced fragmentation. Here, a fragmentation coefficient, γ, is assigned to bridge the unknown correlation between M_{ce} and the increase rate of constitutional supersaturation. The details can be found in Appendix A.

3. Benchmark configuration

The dimension of the casting sample (calculation domain), the boundary, and initial conditions were rigidly derived from the benchmark experiment [7], as shown in Fig. 1. The experiment used two lateral heat exchangers, allowing input/extraction of the heat into/from two vertical sides of the sample. The geometry of the sample was a quasi-two-dimensional rectangular ingot with size $100 \times 60 \times 10\ mm^3$. The stage of melt preheating (homogenization of the melt temperature), which was necessary during experiment, was ignored in the numerical simulation. Thus, the melt was assumed to be homogeneous in temperature before solidification. As solidification started, the imposed temperatures were applied at both lateral side walls (Fig. 1(c)). The temperature difference between the two lateral walls was 40 K, and the cooling rate (CR) was 0.03 K/s. The front/back and top/bottom walls were treated as adiabatic.

The alloy was Sn-10 wt% Pb. A linearized Pb-Sn binary phase diagram, with a constant solute partition coefficient k and a constant liquidus slope m, was used. Other thermodynamic and thermal physical data/properties are listed in Table 1 The transport of equiaxed crystals due to sedimentation played an essential role in this benchmark experiment. The density of solid equiaxed dendrites was reasonably assumed constant ($7950\ kg\ m^{-3}$), but the liquid density was strongly dependent on the solute (Pb) mass fraction [33,34], as is shown in Fig. 2.

Several auxiliary quantities were used to analyse the macrosegregation [35,36]: the mixture concentration, $c_{mix} = (c_\ell \rho_\ell f_\ell + c_c \rho_c f_c + c_e \rho_e f_e)/(\rho_\ell f_\ell + \rho_c f_c + \rho_e f_e)$; macrosegregation index, $c^{index} = (c_{mix} - c_0) \times 100/c_0$; and the global macrosegregation intensity, $GMI = (\iint_{V_{domain}} |C^{index}| d\nu)/V_{domain}$. The model was implemented within the framework of the CFD software, ANSYS-Fluent, Version 14.5. All simulations were performed in parallel

Table 1
Material properties and other parameters.

	Symbol	Units		Ref.
Nominal concentration of alloy (Pb)	c_0	1	0.1	
Liquidus temperature	T_{liq}	K	492.14	[33]
Melting point of solvent (Sn)	T_f	K	505	[33]
Eutectic composition	c_{eu}	1	0.381	[33]
Eutectic temperature	T_{eu}	K	456	[37]
Liquidus slope	m	K	−128.6	[33]
Equilibrium partition coefficient	k	1	0.0656	[33]
Reference density	ρ_{ref}	$kg\ m^{-3}$	7000	[33]
Solid density	ρ_e, ρ_c	$kg\ m^{-3}$	7950	[34]
Specific heat	c_p^ℓ, c_p^e, c_p^c	$J\ kg^{-1}\ K^{-1}$	260	[33]
Thermal conductivity	k_ℓ, k_e, k_c	$W\ m^{-1}\ K^{-1}$	55.0	[33]
Latent heat	L	$J\ kg^{-1}$	6.1×10^4	[33]
Viscosity	μ_ℓ	$kg\ m^{-1}\ s^{-1}$	1.0×10^{-3}	[33]
Liquid thermal expansion coefficient	β_T	K^{-1}	6.0×10^{-5}	[33]
Primary dendritic arm spacing	λ_1	M	2.25×10^{-4}	[38]
Secondary dendritic arm spacing	λ_2	M	6.5×10^{-5}	[33]
Diffusion coefficient (liquid)	D_ℓ	$m^2\ s^{-1}$	4.5×10^{-9}	[39]
Diffusion coefficient (solid)	D_c, D_e	$m^2\ s^{-1}$	1×10^{-12}	[39]
Initial temperature	T_0	K	492.14	[33]
Gibbs-Thomson coefficient	Γ	m K	6.5×10^{-8}	[38]
Fragmentation coefficient	γ	1	0.1	

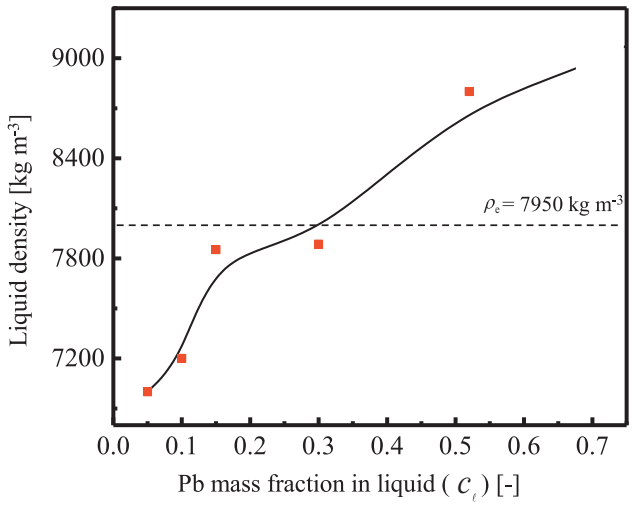

Fig. 2. Melt density as function of solute (Pb) mass fraction in the Sn-Pb alloy [33,34].

on a high-performance cluster (2.6 GHz, 12 cores). It takes approximately 30 days for a three-dimensional (3D) simulation and approximately 10 days for a 2D case.

4. Results

4.1. Solidification sequence

The calculated solidification sequence is shown in Fig. 3. To assist in the result description, the global solidification and melt flow patterns are schematically drawn in Fig. 3(a.x). A full 3D calculation was performed, but here only the result on a vertical section at z = 0.003 m is presented. The reason for showing the result on this section rather than on the symmetry section z = 0.0 m is that no obvious segregation channel appears on the symmetry section. Although the casting configuration is quasi-two-dimensional, the calculated mesosegregation (channel segregation) has the nature of full 3D, i.e. the main channel does not appear in the casting centre, but quite close to the casting surface. The time is accounted from the start of the cooling stage (Fig. 1(c)).

At 30 s, a clockwise thermal convection with maximum velocity 3.7×10^{-2} m/s developed (Fig. 3(b.1)). As the superheat of the melt

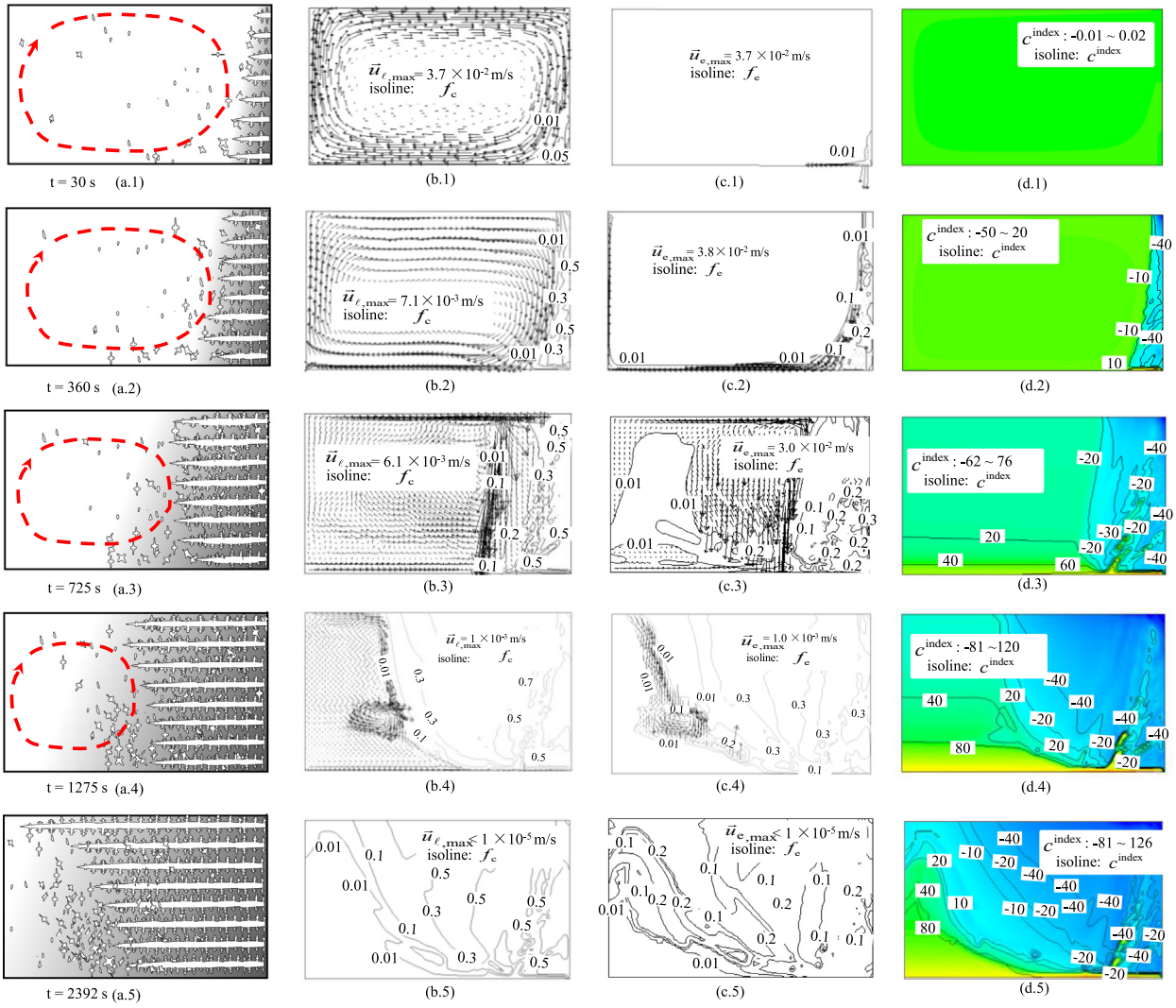

Fig. 3. Solidification sequence of the benchmark (on the plane z = 0.003 m): (a.x.) Schematic of solidification regions and global melt flow pattern, (b.x.) liquid velocity overlaid with f_c isoline, (c.x.) equiaxed velocity overlaid with f_e isoline (d.x.) contour of the macrosegregation index (c^{index}). c^{index} are shown in the colour scales with blue for the minimum (or negative extreme), and red for the maximum (or positive extreme).

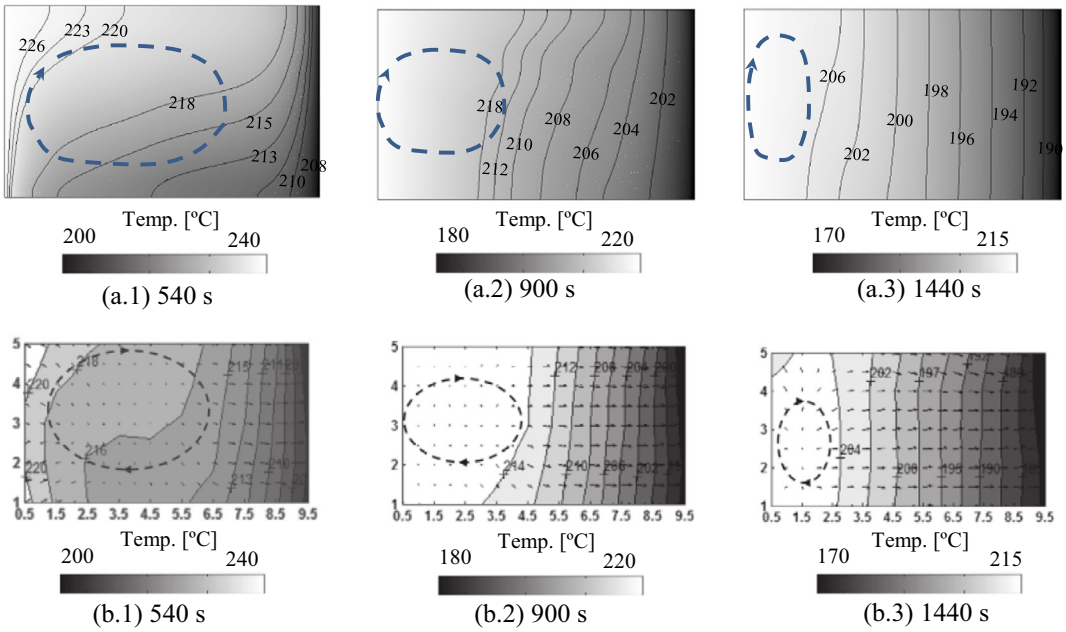

Fig. 4. Comparison of the temperature field on the symmetry plane z = 0.0 at t = 540, 900, and 1440 s from the beginning of solidification between simulation (a.x) and experiment (b.x). (b.x) are reprinted from publication [7], with permission from Elsevier.

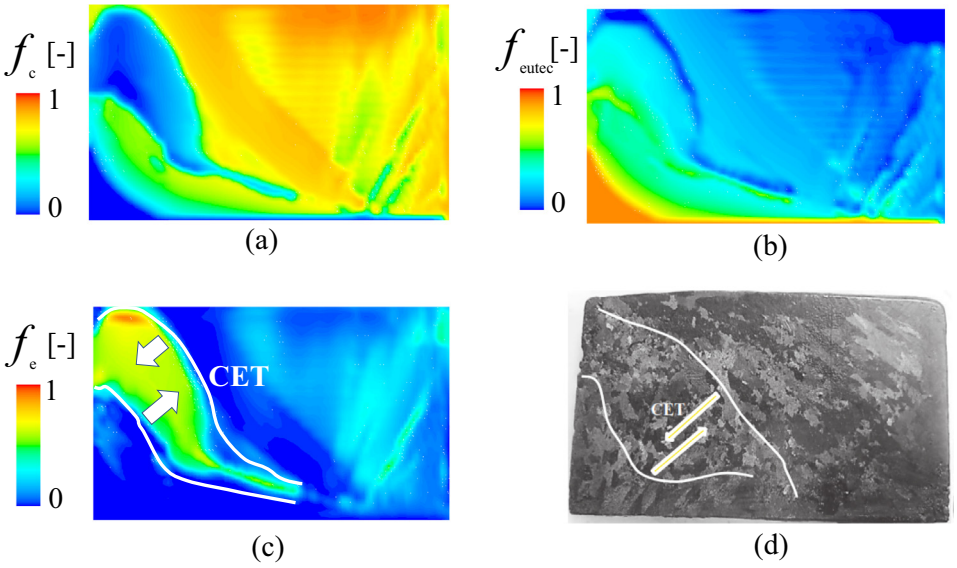

Fig. 5. As-cast structure: simulation results of volume fractions of (a) columnar, (b) rest eutectic, and (c) equiaxed phases; (d) metallography of the as-cast structure. (d) is reprinted from publication [7], with permission from Elsevier.

is extracted from the cold wall (right side) and the temperature there drops gradually below the liquidus temperature, the columnar trunks start to grow. A columnar-liquid mushy zone forms, and in the mushy zone, equiaxed crystals are produced because of the fragmentation. Equiaxed crystals have the tendency to sediment on the bottom because the density of the equiaxed phase is larger than that of the liquid. The lower-right corner is the place where equiaxed crystals first accumulate (Fig. 3(c.1)). At this early stage of solidification, the macrosegregation over the domain is negligibly small (Fig. 3(d.1)).

At 360 s, the columnar phase region on the right side of the benchmark extends leftwards (Fig. 3(a.2)–(b.2)). The velocity of the liquid decreases dramatically, and its maximum value is approximately 7.1×10^{-3} m/s. In the mushy zone, the liquid can flow through the columnar dendrites, initializing the segregation channels (Fig. 3(b.2) and (d.2)). Equiaxed crystals are produced continuously near the columnar front by fragmentation, but they are brought into the bulk region. The maximum velocity of the equiaxed crystals is approximately 3.8×10^{-2} m/s. It is larger than that of the liquid, and the region with high velocity is located near the columnar front. The accumulated equiaxed region is spread along the bottom surface of the benchmark (Fig. 3(c.2)).

From 360 s to 725 s, the liquid velocity deceases gradually. More segregation channels are observed in the columnar region (Fig. 3(b.3) and (d.3)). More equiaxed crystals are produced in the region near the columnar tip front (Fig. 3(a.3)). In the middle bottom region of the benchmark, the equiaxed phase forms a packed zone. In the bulk region near the hot wall, equiaxed crystals

float up, or sink down to the lower-left region where remelting of the crystals occurs (Fig. 3(c.3)).

As solidification proceeds to 1275 s, the columnar front continues to grow (Fig. 3(a.4)), and more segregation channels form in the columnar region (right) (Fig. 3(d.4)). Solute (Pb) enrichment in the liquid phase increases the liquid density, hence decreasing the density difference between the liquid and equiaxed phase. It becomes easier for liquid to sweep the equiaxed crystals with the upward melt flow. A portion of equiaxed crystals is even brought upwards by a vortex (Fig. 3(b.4)–(c.4)). Some small equiaxed crystals are brought upwards to the upper-left corner region. They grow, and then settle down. One can also see that some newly formed crystals by dendrite fragmentation attach to the packed equiaxed network in the bottom near the vortex (Fig. 3(c.4)). The solute enriched melt, which becomes denser and heavier, starts to accumulate in the bottom-left region of the benchmark, resulting in a positive macrosegregation in the lower-left corner (Fig. 3(d.4)).

At 2392 s, the velocities for both liquid and equiaxed phases vanish. The right part of the benchmark is composed of the columnar phase with negative macrosegregation and positive segregation channels. The lower-left part is dominated by a solute-enriched phase (rest eutectic) with positive macrosegregation. There is an equiaxed region on the upper-left corner (Fig. 3(c.5)), which extends to the middle bottom region. The solidification does not end yet, and the final as-cast structure and macrosegregation remain nearly unchanged during the rest solidification.

4.2. Comparisons with the experimental measurements

4.2.1. Temperature field

The calculated temperature field is compared with the experimental measurement (Fig. 4). As the temperature gradient builds up during the early stage of solidification (Fig. 4(a.1)), a clockwise convection forms and distorts the isotherms. Afterwards, as the solidification front advances and the flow magnitude decreases, the isotherms gradually become vertical (Fig. 4(a.2) and (a.3). The simulation results agree well with the experimental measurement (Fig. 4(b.1)–(b.3)). However, the global temperature, especially near the hot side wall, is slightly overestimated by the simulation. The reason may be the heat loss through the front/back and top/bottom walls, which is ignored by the numerical simulation. In the experiment, minor heat loss from those walls would occur [5,40].

4.2.2. As-cast structure

Comparison of the as-cast structure between simulation and experiment is shown in Fig. 5. The general appearance of them is quite similar. The upwind tiled columnar structure region is located in the left side. A small second columnar structure region is observed in the lower-left corner, where the volume fraction of rest eutectic is predicted quite high by the simulation. The equiaxed structure is located in the upper-left region, which extends to the middle bottom. The equiaxed zone is enclosed between two lines, which indicate the CET.

4.2.3. Macrosegregation

The macrosegregation between simulation and experiment is compared in Fig. 6. Numerically, the most positive macrosegregation (up to 25 wt% Pb) is located near the left side wall where the melt solidifies at the late stage, and the negative macrosegregation is located in the upper- right side of the benchmark. Near the lower-right corner, several segregation channels are observed in Fig. 6(a). Pb concentration in the segregation channels reaches 16 wt%. The numerically predicted segregation map (Fig. 6(a)) agrees qualitatively with the experimental results, as measured by two different methods. Fig. 6(b) shows the Pb distribution as measured by chemical analysis with technical inductively coupled plasma (ICP). It is mapped on the basis of 50 discrete measurements over the longitudinal section of the benchmark. Fig. 6(c) shows X-radiography of the as-solidified benchmark. Mesosegregation (channel segregates) can be clearly observed. The contrast of the X-radiography can provide only a qualitative evaluation of the relative Pb concentration. A quantitative segregation map (Fig. 6(d)) is made through digital processing of the X-radiography, and then calibrated by the chemically analysed quantities from Fig. 6(b).

A 3D view of segregation channels is presented by the isosurface of 12 wt% Pb (Fig. 7). The channels form preferentially along the mould walls. Only some small discontinuous channel

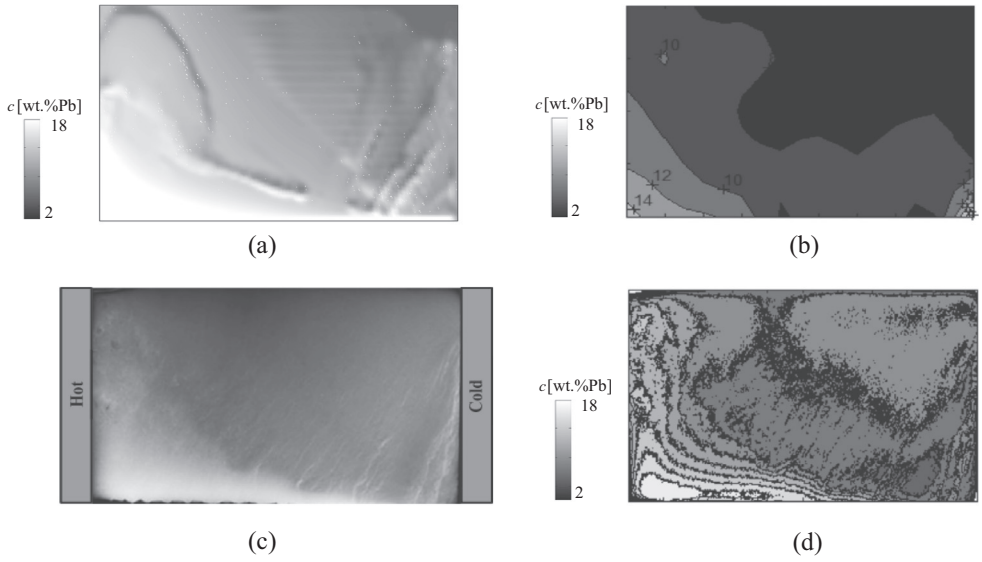

Fig. 6. Macrosegregation: (a) simulated macrosegregation (wt.% Pb) on the plane z = 0.003 m, (b) Pb concentration map measured by the chemical method coupled with technical inductively coupled plasma, (c) X-radiography of the as-solidified benchmark, and (d) Pb concentration map digitally processed from (c), and calibrated by the concentration value in (b). (b), (c) and (d) are reprinted from publication [7], with permission from Elsevier.

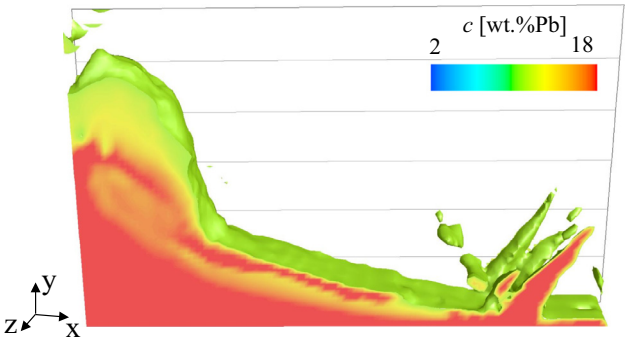

Fig. 7. 3D view of iso-surface of 12 wt% Pb, coloured by Pb-concentration from 2 wt % (blue) to 18 wt% (red). (For interpretation of the references to colour in this figure legend, the reader is referred to the web version of this article.)

pieces in the casting centre are found. Most channels are in the form of tubular structures. There are also some lamellar-structured channels, which connect the bottom Pb-enriched zone.

Views of macrosegregation in slices perpendicular to the front/back walls at nine positions, corresponding to 10, 20, 30, 40, 50, 60, 70, 80, and 90 mm from the cold wall of the as-solidified benchmark, are shown in Fig. 8. X-radiographs of the nine transverse-cut slices were made, and compared with the numerical simulation. The experimental slices were made perpendicularly to the front/back walls, but the views of X-radiographs were turned by 90°. Note that this comparison can be made only qualitatively, because each X-radiograph represents an integration of the X-ray signal through the thickness of each slice (5–6 mm), whereas the numerical result is the segregation map on the section. The contrast intensity of the X-radiographs is attenuated by the averaging over the thickness, probably resulting in the ignorance of the mini channels there. Generally, the simulation-experiment agreement is good. The global locations of the intensive Pb-enriched areas as predicted by simulation coincide with lighter areas as detected by the X-radiographs. The fact of the occurrence of channel segregates and their locations seem to agree with each other as well. The main differences between the simulation and the experiment are as follows. The concentrated positive segregation of Pb in the lower-left corner region seems to be overestimated by the simulation, and the transition from the high Pb-enriched region to the lower Pb-enriched region is numerically calculated more clearly than the experimental result (X-radiographs show a smoother transition from the very light region to the grey region). Exact locations of the segregation channels do not match the experimental results, and the average size (diameter) of the channels is also overestimated by the numerical simulation. It is known that one reason for this mismatch is the mesh size, which was discussed in previous reports [21,22].

Quantitative comparison of the macrosegregation profiles along horizontal lines (x direction) were made between the simulation and experiment (Fig. 9). Experimental measurements of Pb concentrations were made by the chemical method coupled with ICP. Fifty samples were extracted by drilling holes from the as-cast benchmark, at height y = 0.05, 0.04, 0.03, 0.02, and 0.01 m. This means that for each height, ten samples were drilled with equal intervals along the x direction. The mass used for chemical analysis was approximately 200 mg from each drilled sample. It is assumed that the measured Pb-concentration represents the mean value of the drilled sample, i.e. the mean Pb-concentration through the sample thickness (z direction). In order to make the simulation-experiment comparison meaningful, the simulation curves of Fig. 9 were also made by averaging the values through the sample thickness. In principle, the experimental points (data) and the simulation curves show a similar distribution tendency, but the

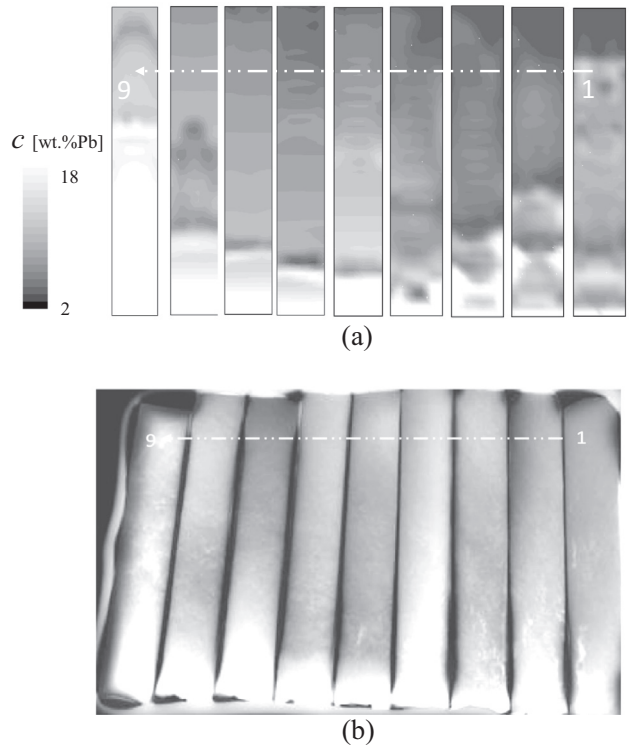

Fig. 8. Views of macrosegregation in slices perpendicular to the front (or back) side wall at positions 1–9, corresponding to 10, 20, 30, 40, 50, 60, 70, 80, and 90 mm from the cold wall: (a) Contours of Pb concentration predicted by simulation, and (b) X-ray photographs of the slices centred on the abovementioned positions (lighter colours correspond to Pb-rich zones). (b) is reprinted from publication [7], with permission from Elsevier.

numerical simulation seems to have overestimated the macrosegregation intensity. The calculated maximum positive segregation in the lower-left region (Fig. 9(e)) and the maximum negative segregation in the upper-right region of the benchmark (Fig. 9(a)) are larger than the experimental results. Additionally, some simulation curves (e.g. Fig. 9(e)) show clear fluctuation, sometimes varying between local minimum and maximum, indicating the line crossing the CET border or crossing the segregation channels; however, this kind of fluctuation cannot be seen experimentally. There is only one experimental point (close to the cold wall in Fig. 9(e)) that reaches a concentration of 20 wt% Pb, indicating probable channel segregation. From the X-radiographs (Fig. 6(c) and (d)), a few more channels can be identified. Those channels were obviously missed by the chemical analysis in Fig. 9.

5. Discussion

To understand the formation of the as-cast structure and macrosegregation, analyses of the numerical results and numerical parameter studies were made. In the previous section, a 3D simulation result was presented. This section is mostly based on the 2D calculations for purposes of enhancing the computational efficiency. Numerical factors, including the dimension (2D/3D) and mesh size, would influence the calculation accuracy [41]. A comparison between 3D and 2D calculations is shown in Fig. 10. Details about the distribution of the equiaxed phase, and the number and shape of the segregation channels, are slightly different between the 3D and 2D calculations. However, the global distribution of the as-cast structure, macrosegregation, and occurrence and location of segregation channels are quite similar. Sensitivity of the simulation result to the grid size is further analysed in §5.4.

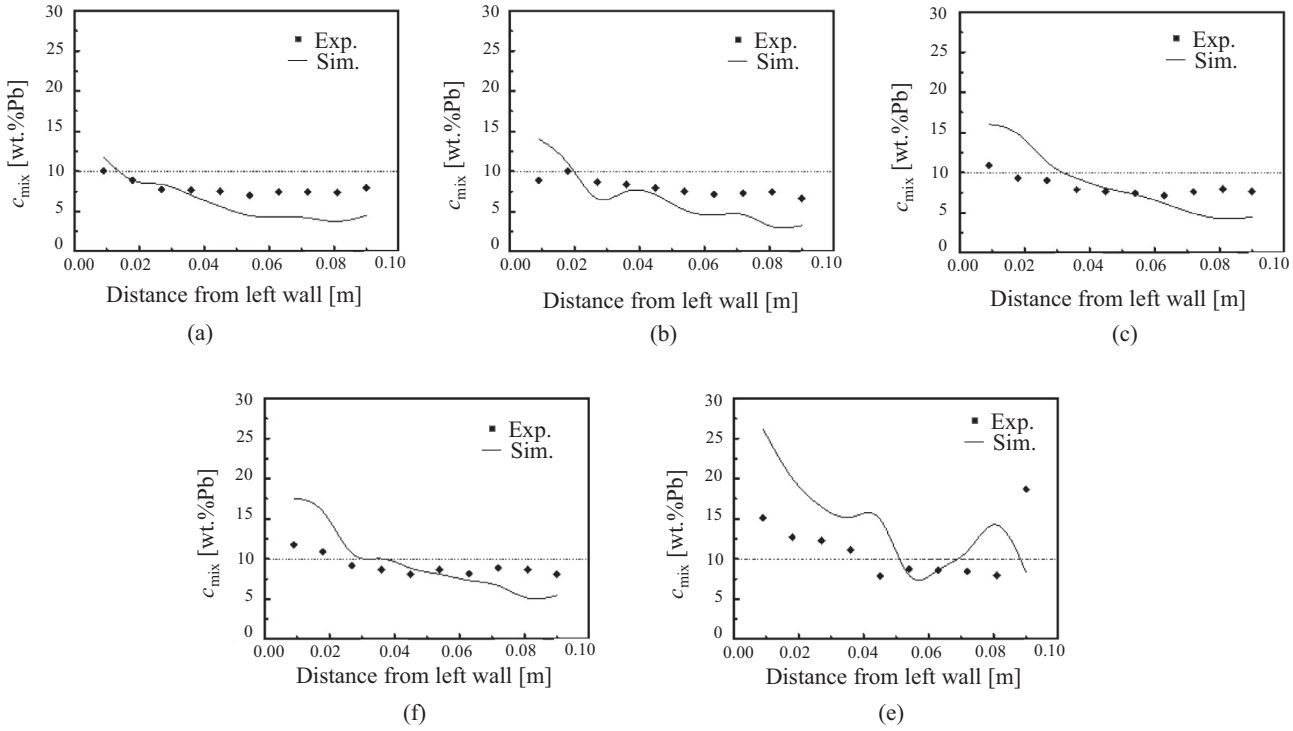

Fig. 9. Comparison of Pb-concentration obtained by ICP analysis (squares) with the simulation along the horizontal lines (x direction): (a)–(f) correspond to five different heights at y = 0.05, 0.04, 0.03, 0.02, 0.01 m. The simulation curves are post-processed by averaging the values through the thickness (z direction).

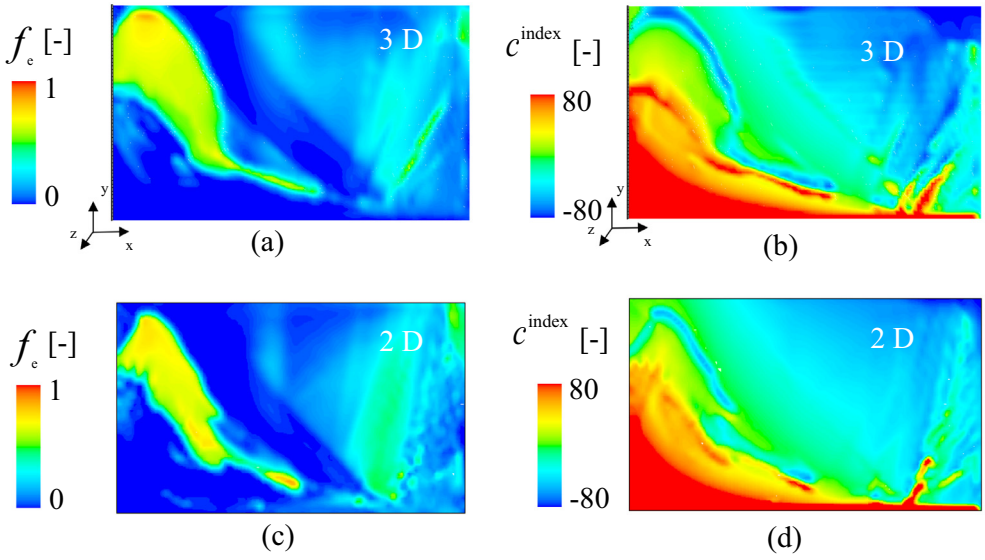

Fig. 10. Comparison of 3D and 2D simulations: (a) f_e and (b) c^{index} contours on the plane z = 0.003 m of the 3D simulation, and (c) f_e and (d) c^{index} contours of 2D simulation. Mesh sizes for both simulations are the same (1 mm).

5.1. Origin of equiaxed crystals by fragmentation

The production rate of fragments is quantified by N_{frag}, which is derived from the fragmentation-induced columnar-to-equiaxed mass transfer rate [23], as calculated by the formula $M_{ce} = -\gamma \cdot \vec{u}_\ell \cdot \nabla c_\ell \cdot \rho_e$, with an assumption of the size of newly created fragments ($d^0_{e,frag}$) equal to $\lambda_2 f_c$. Details about the fragmentation model, i.e. formula precisely, are described in Appendix A. This formula is suggested on the concept that the solute-driven remelting is the dominant mechanism for fragmentation [28–32], and transport of the solute-enriched melt by the interdendritic flow in the columnar-growth direction (or against the ∇c_ℓ direction) enhances the remelting. Additionally, the flow in the columnar-growth direction is a necessary condition to transport fragments out of the mush zone [42].

A detailed analysis of $\vec{u}_\ell$, ∇c_ℓ and the production rate of fragments N_{frag} is made in Fig. 11. The dendrite fragments are mostly produced near the columnar tip front. A global flow pattern is in the clockwise direction and it has the largest velocity near the columnar tip front (Fig. 11(a) and (b)). The columnar tip front is approximated by $f_c = 0.02$. Along the columnar tip front, the flow direction ($\vec{u}_\ell$) is slightly tilted outwards from the columnar mushy

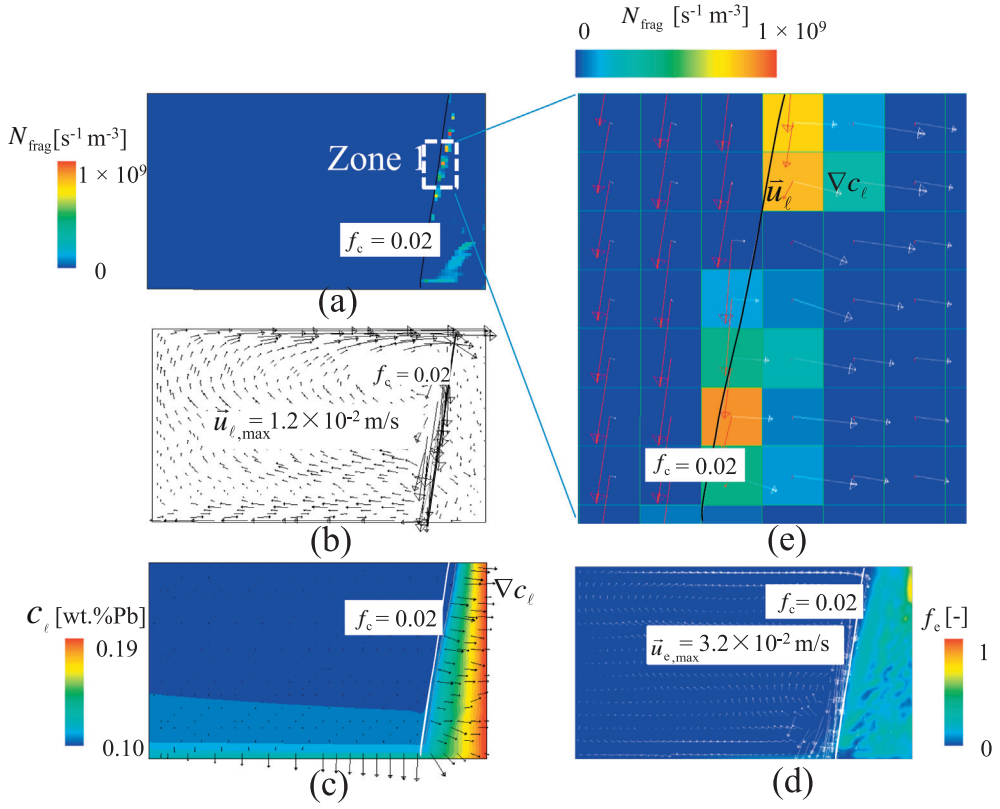

Fig. 11. Formation of equiaxed crystals by fragmentation (at 600 s). (a) Distribution of production rate of fragments N_{frag} with columnar tip front approximated by $f_c = 0.02$; (b) liquid velocity $\vec{u}_\ell$; (c) liquid concentration(c_ℓ) overlaid with vector ∇c_ℓ; (d) equiaxed volume fraction $f_e$and its velocity $\vec{u}_e$; (e) zoomed-in view of N_{frag} in Zone 1 overlaid with the liquid velocity $\vec{u}_\ell$ (red) and liquid concentration gradient ∇c_ℓ (white). (For interpretation of the references to colour in this figure legend, the reader is referred to the web version of this article.)

zone (Fig. 11(e)). The direction of ∇c_ℓ is always towards the columnar mushy zone, i.e. against the columnar tip growth direction (Fig. 11(c)). This kind of flow favours the fragmentation. A zoomed-in view (Zone 1) of the fragmentation region (Fig. 11(e)) provides more details about the distribution of N_{frag}. The liquid velocity and liquid concentration gradient are shown in vectors: $\vec{u}_\ell$ in red and ∇c_ℓ in white. The angle between the two vectors indicates the possibility of fragmentation. When it is larger than 90°, fragmentation may occur. No fragments can be produced when it is smaller than 90°. The non-homogenous distribution of $N_{frag}$is caused mainly by the instable flow along the columnar tip front. Both the velocity magnitude and flow direction oscillate along the columnar tip front, causing the non-homogenous distribution of N_{frag}. Note that one modelling parameter is introduced: the fragmentation coefficient γ. All unknown factors contributing to fragmentation, such as the curvature effect of the dendrites, latent heat-induced thermal fluctuation, and diffusion in the interdendritic melt, were included in the single γ. This parameter should be determined experimentally. The previous numerical parameter study [23] by varying γ (from 0.01 to 10.0) suggested a constant value (0.1) for the alloy Sn-10 wt% Pb. The simulation-experiment agreement for the current benchmark verifies that the value of 0.1 for γ is a reasonable choice for this alloy.

5.2. Formation of the equiaxed zone

As shown in Fig. 5(d), an accumulated equiaxed zone was obtained in the upper-left corner region of the as-solidified benchmark casting, and this region extends to the middle bottom. Similar results are predicted numerically (Fig. 5(a)–(c)). This is due to the transport of the equiaxed crystals. As shown in Figs. 3 and 11, all equiaxed crystals originate by fragmentation near the columnar tip front. The fragmentation-induced crystal fragments, i.e. equiaxed crystals, are transported out of the columnar mushy zone. They tend to sink down along the columnar tip front because its density is higher than that of the liquid melt, but in the meantime the melt flow also tries to bring them into the bulk region (left side). Because the density of the melt is strongly dependent on the solute enrichment of the melt (Fig. 2), the equiaxed crystals can settle down or float up through the balance of the flow-induced drag force and the gravity-driven sedimentation. In the early stage of solidification, the density of the solid (ρ_e) is much larger than that of the melt (ρ_ℓ); hence, the equiaxed crystals are prone to accumulate in the bottom region. In the late stage, however, with the gradual enrichment of Pb in the melt, the density difference ($\Delta\rho_{e\ell} = \rho_e - \rho_\ell$) becomes sufficiently small so that the drag force by melt flow can easily overwhelm the buoyancy force.

A detailed analysis of the crystal movement and the melt flow in the period from 1100 s to 1540 s is shown in Fig. 12. The newly formed fragments/equiaxed crystals along the columnar tip front sink downwards, driving a clockwise melt flow in the bulk melt pool. Both liquid and equiaxed phases are coupled by the drag force, which is according to Wang et al. [43]. As the downward melt stream along the columnar tip front meets the bottom region, it is 'forced' to change the direction. This sharp change of the flow direction causes to form a small clockwise vortex (Fig. 12(a.x)). This vortex is located in the low-right corner of the bulk melt pool. It is this vortex that carries a certain amount of equiaxed crystals away from the columnar tip front (Fig. 12(b.x)). In the 'eye' of the vortex, a relatively high volume fraction of equiaxed phase is distributed. As time proceeds, the whole area of the melt pool

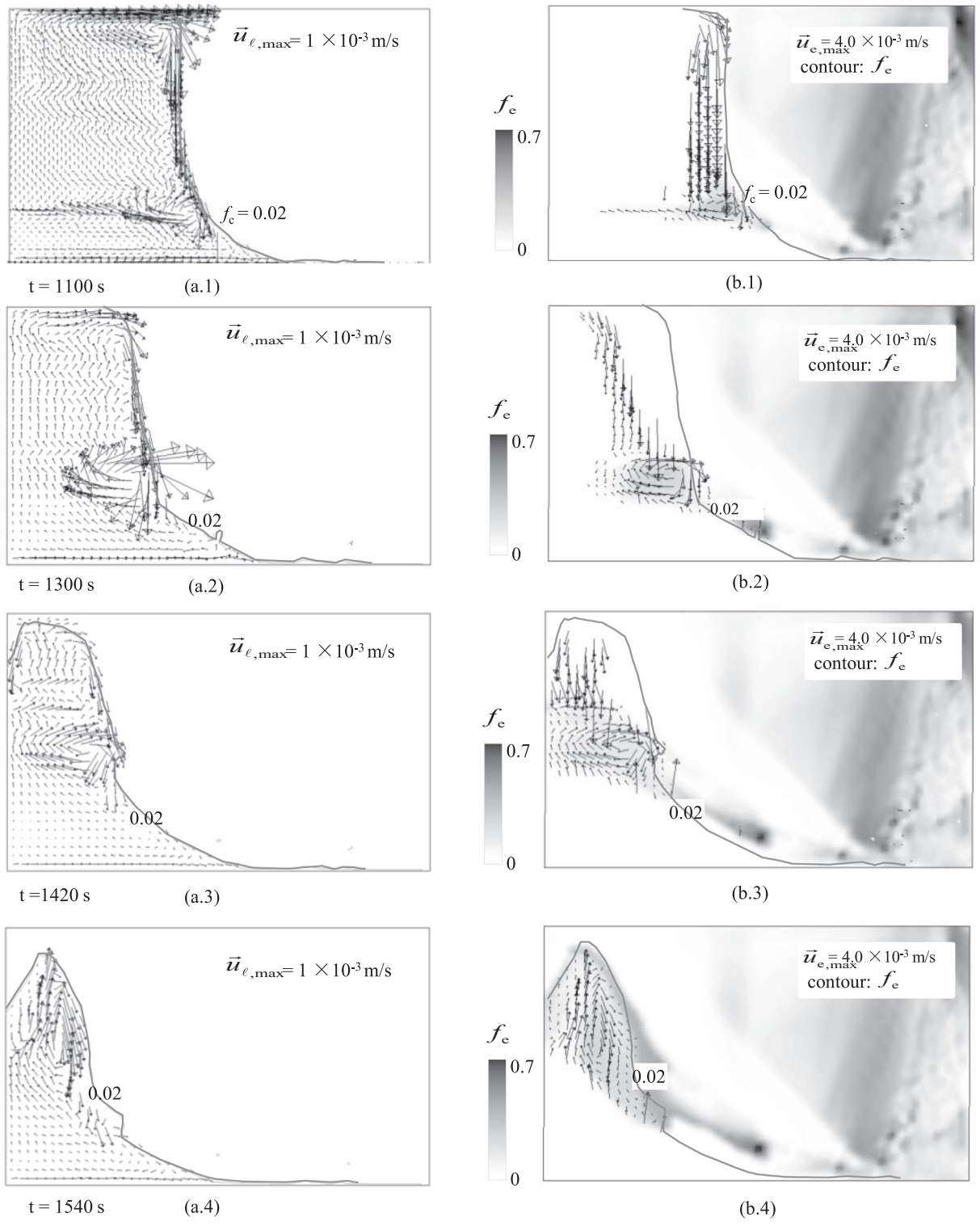

Fig. 12. Transport of crystal crystals during solidification in the period from 1100 s to 1540 s: (a.x) liquid velocity $\vec{u}_\ell$overlaid with the isoline f_c = 0.02. Liquid velocity is shown in the region where the liquid volume fraction f_ℓ is between 0.1 and 1; (b.x) distribution of f_e overlaid with equiaxed velocity $\vec{u}_e$and isoline f_c = 0.02. Equiaxed velocity is shown only in the region where f_e is between 0.001 and 1.

shrinks gradually (Fig. 12(a.2)–(a.4)). Correspondingly, the small vortex moves from the middle bottom region towards upper-left part of the benchmark, leaving a trail of distribution band of equiaxed phase (Fig. 12(b.2)–(b.4)). It can be anticipated that the crystal-carry vortex contributes significantly to the accumulated equiaxed zone of Fig. 5.

To demonstrate the role of the crystal movement in the formation of the as-cast structure, two extreme cases were calculated. Case (a) assumed a constant $\Delta\rho_{e\ell} = -150$ kg/m^3, i.e. the equiaxed is slightly lighter than the melt; Case (b) assumed a constant $\Delta\rho_{e\ell}$ = 950 kg/m^3, i.e. the equiaxed is significantly heavier than the melt. Both cases ignored the density change of the melt with the Pb

enrichment. Calculation results are shown in Fig. 13. Although the melt flow patterns for both cases are quite similar, the movements of the equiaxed crystals are completely different; hence, different as-cast structures are predicted. In Case (a), fragmentation-induced equiaxed crystals are first brought out of the columnar mushy zone, and then most of them float up to the top of the benchmark. In Case (b), fragmentation-induced equiaxed crystals try to settle down immediately, but most of them are captured in the columnar phase region. Only a small portion of them are brought out of the columnar mushy zone, and then are transported and accumulate in the left corner region of the benchmark. Obviously, none of these cases with a constant $\Delta\rho_{e\ell}$ can 'reproduce' the as-cast structure (Fig. 5(d)) as obtained experimentally.

5.3. Channel segregates (mesosegregation)

Channel segregates, also called mesosegregation or segregation channels, start and grow in the region of the columnar tip front (Fig. 3). In the as-solidified benchmark, those channel segregates are located in the lower part of the columnar structure (Figs. 5 and 6). A previous study by the current authors [21,22] found that channel segregates develop in two steps, i.e. the onset and the channel growth. Onset of the channel is caused by the mush (or convection) instability, which can be analysed in terms of the mush zone Rayleigh number (*Ra*) [44,45]. If *Ra* is larger than a critical value (0.12–0.24), a channel would initialize. However, the *Ra* criterion alone is not a sufficient condition to predict the channel formation. The onset channel must continue to grow into a stable channel by the resulting interdendritic flow-solidification interaction. This flow-solidification interaction can be analysed by the interaction term, $\vec{u}_\ell \cdot \nabla c_\ell$. The sign of this term, $\vec{u}_\ell \cdot \nabla c_\ell$, can be used to distinguish two solidification regions: a suppressed solidification region, where the sign of the flow-solidification interaction term is negative (flow is in the opposite direction of the liquid concentration gradient); and an accelerated solidification region, where the sign of the flow-solidification interaction term is positive (flow is in the same direction of the liquid concentration gradient). Channels can occur only in the suppressed solidification region, where an increase in local flow caused by a flow perturbation is reinforced by the resulting suppressed solidification. This scenario occurs in the lower part of the columnar tip front region. In this situation, the flow becomes unstable and channels continue to grow. Channels do not form in the accelerated solidification region, where an increase in local flow intensity due to flow perturbation is throttled by the resulting accelerated solidification. In this latter case, flow perturbation is stabilized by flow-solidification interactions, and it does not matter whether the *Ra* criterion for the onset of channels is fulfilled. For example, in the upper part of the columnar tip front region, the *Ra* criterion could also be fulfilled, but no channel would occur there.

This paper will not repeat the analysis of the previous work [21,22], but a suppressed solidification region, where channels develop, is shown with more detail (Fig. 14). Channels are characterized by the lower solid fraction region, corresponding to the region of high c^{index}. The positive direction of ∇c_ℓ during this stage of solidification is always rightward (Fig. 11(c)); the flow in the channel is left-downward, as shown in Fig. 14(a.2). The sign of $\vec{u}_\ell \cdot \nabla c_\ell$ in the channel is negative, i.e. the solidification is suppressed. In the neighbouring region (channel wall), however, the flow is conducted towards the channel, which is much more permeable. The sign of $\vec{u}_\ell \cdot \nabla c_\ell$ in the neighbouring region (channel wall) is no more negative, i.e. solidification might be accelerated there. With this kind of flow-solidification interaction, the channel becomes stable.

The view of the transverse section (Fig. 14(a.3)–(b.3)) shows that the channels occur preferentially near the wall, which coincides with other numerical studies [6,46] as well as with the current benchmark (Fig. 8(b)) and other experiments [47].

5.4. Grid sensitivity

Calculations with four mesh sizes (0.8, 1.0, 1.5, and 2.0 mm) were performed. Fig. 15 shows the equiaxed phase distribution and macrosegregation at the end of solidification. A CET line

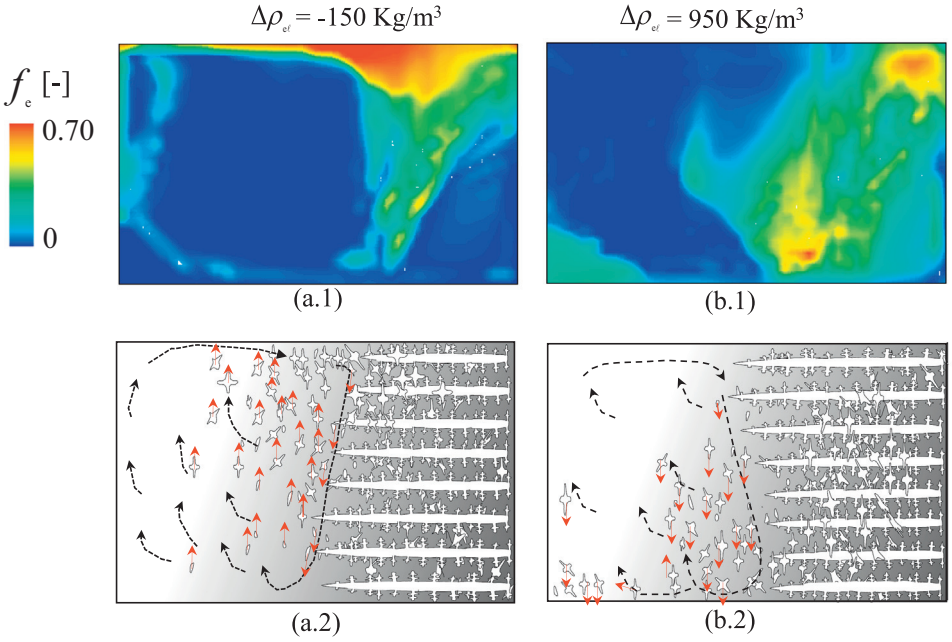

Fig. 13. Influence of density difference between equiaxed phase and melt ($\Delta\rho_{e\ell}$) on the formation of as-cast structure. Two cases are calculated: (a.x) with $\Delta\rho_{e\ell} = -150$ kg m^{-3}; (b.x) with $\Delta\rho_{e\ell} = 950$ kg m^{-3}. The upper row (a.1) and (b.1) are the simulation results of the f_e distribution in the as-solidified benchmark; the lower row (a.2) and (b.2) are schematics of the melt flow and equiaxed movement (black dashed lines indicate the circulation of melt flow and red arrows indicate the moving direction of equiaxed crystals).

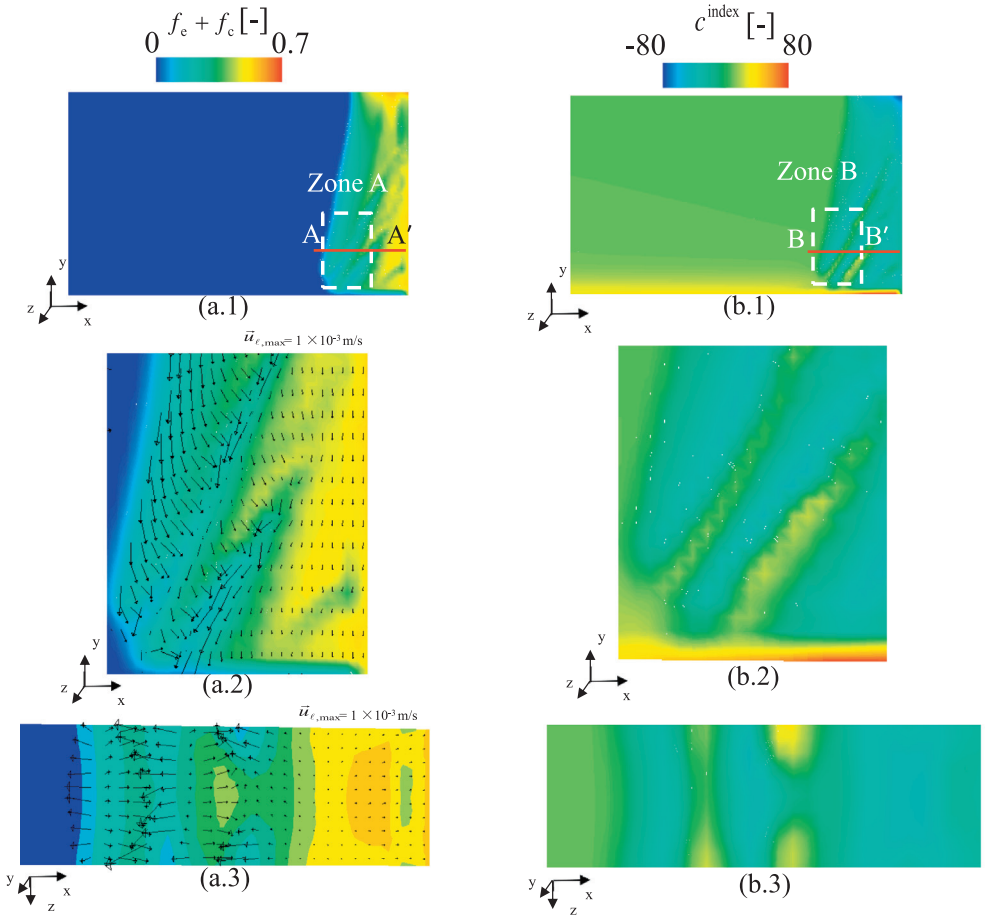

Fig. 14. Analysis of channel segregation during the early stage of solidification (at 700 s): (a.1) solid fraction ($f_e + f_c$) on the plane z = 0.003 m; (a.2) zoomed-in view (Zone A), superimposed with liquid velocity; (a.3) solid fraction on the transversal section contour along A–A′; (b.1) macrosegregation (c^{index}) on the plane z = 0.003 m; (b.2) zoomed-in view (Zone B); (b.3) macrosegregation on the transversal section along B-B'. This result is taken from the 3D calculation.

separates the columnar and equiaxed regions (Fig. 15(a.x)). Macrosegregation distributions are compared in Fig. 15(b.x). It does not seem possible to possess a grid-independent result, especially regarding to the distribution of equiaxed area and the details of the channel segregates (mesosegregation), but the global as-cast structure and macrosegregation pattern are similar for all cases. The area of the equiaxed zone, as bordered by the CET line, remains nearly unchanged when the mesh size is smaller than Δx = 1.5 mm. All cases have predicted the occurrence of channel segregates in the lower-right corner of the benchmark (columnar structure region). A tendency is clear, that with the decrease in grid size from 2.0 to 0.8 mm, the modelling results of the macrosegregation distribution and segregation intensity tend to converge. The c^{index} value for all cases ranges from −86 to 230. The c^{index} range does not significantly change when the mesh size decreases to smaller than Δx = 1.0 mm. The global macrosegregation intensity (GMI) reflects the overall macrosegregation intensity in the domain, and it seems to approach a convergent result (60.7) when the mesh size is smaller than 1.0 mm.

One can safely conclude that the mesh size of 1 mm, as used for this study, can reliably resolve the global as-cast structure and macrosegregation pattern, and even predict the occurrence (or probability/risk of occurrence) of channel segregates. Fine details of the channel segregates, i.e. the number of channels and segregation intensity in the channels, are not solvable with the current mesh resolution. A similar conclusion was also drawn in other studies [21,22,48]. One origin of this mesh sensitivity of the channel segregates might be the flow in the high liquid volume fraction (in the front of the columnar mushy zone), which is highly sensitive to the mesh size [17].

6. Conclusions

A solidification benchmark experiment based on Sn-10 wt% Pb alloy as performed at the SIMAP Laboratory in Grenoble, France [7] was numerically 'reproduced' by a mixed columnar-equiaxed solidification model [9]. The experiment-simulation agreement in the temperature evolution, as-cast structure, and macro- and mesosegregation further verified the numerical model. By analysis of the modelling results, the following knowledge/conclusions were obtained:

(1) Understanding of the formation of the as-cast structure (mixed columnar-equiaxed), as observed experimentally, was improved. The columnar structure developed first from the cold wall. The fragmentation-induced equiaxed crystals are transported away from the front region of the columnar zone by the melt flow. Those crystals can grow or re-melt during the movement. The equiaxed crystals settle down and float up through the balance of the flow-induced drag force and the gravity-driven sedimentation. The equiaxed crystals, interacting with the growing columnar structure, lead to CET and form the final as-cast structure.
(2) For the alloy (Sn-10 wt% Pb) considered in this benchmark experiment, the density variation of the melt with the Pb enrichment plays a critical role in the movement (transport)

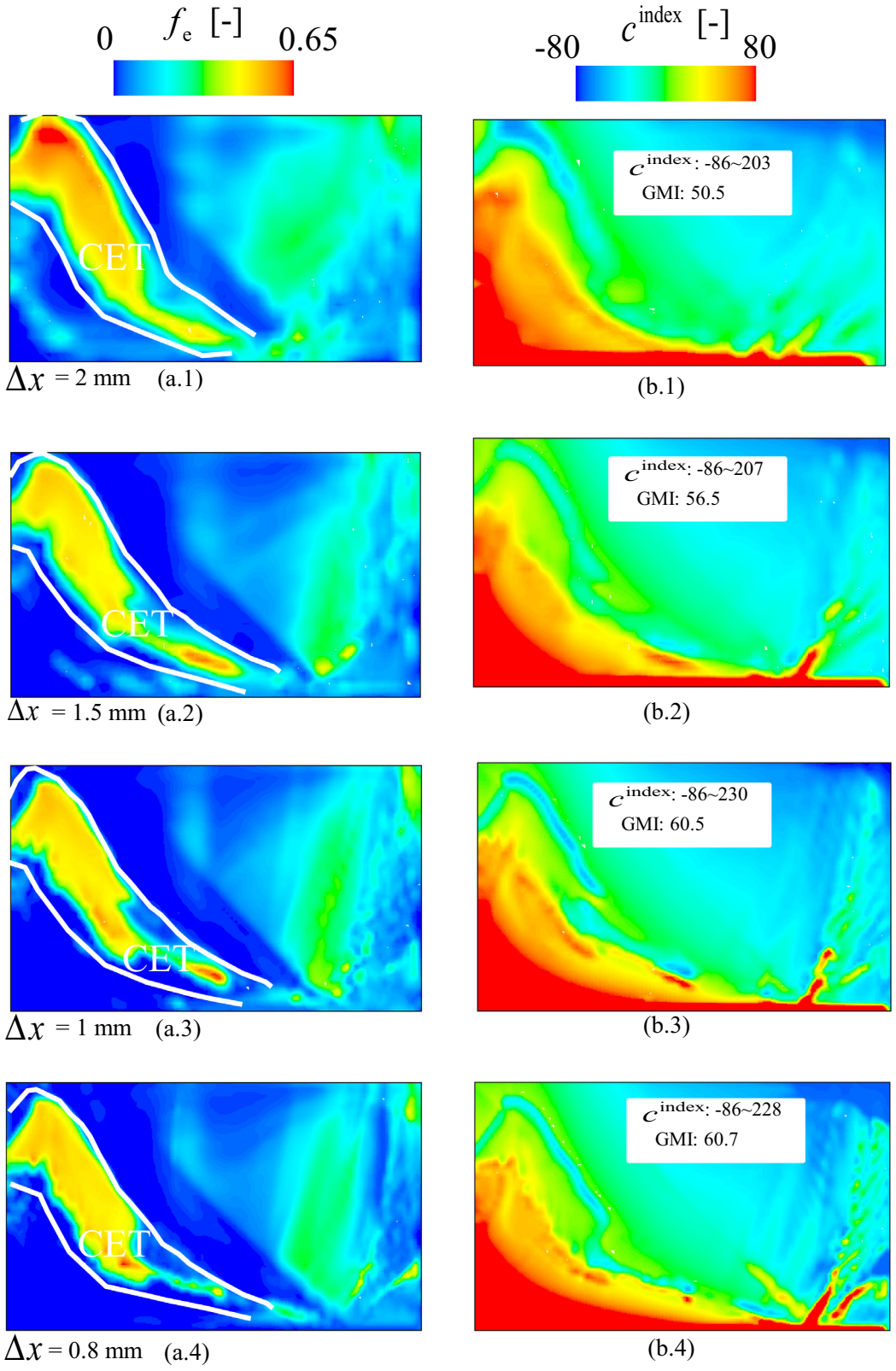

Fig. 15. Influence of mesh size (0.8, 1.0, 1.5, 2.0 mm) on the as-cast structure and macrosegregation: (a.x) f_e distribution with bold lines for the CET; (b.x) c^{index} map and global macrosegregation intensity (GMI) value.

of equiaxed crystals. The equiaxed crystals are normally denser than the melt, and tend to settle downwards. With the Pb-enrichment during solidification, however, the melt becomes gradually denser as well. The reduced density difference between the solid and the Pb-enriched melt favours the upward motion of the crystals, because of the drag force

as imposed by the upward melt flow. If this Pb concentration-dependent density variation of the melt were ignored, the experimentally observed as-cast structure would not be 'reproducible' numerically.

(3) Because crystal fragmentation was found to play a critical role in the origin of equiaxed crystals in this benchmark experiment [7], the mixed columnar-equiaxed model was extended for fragmentation [23]. The modelling concept for fragmentation is that solute-driven remelting is the dominant mechanism for fragmentation [28–32], and transport of the solute-enriched melt by the interdendritic flow in the columnar-growth direction (or against the ∇c_ℓdirection) enhances remelting. Although further experimental evaluations are desirable, the first simulation-experiment comparison with a satisfactory agreement, concerning the result of as-cast structure and global macrosegregation pattern, provides convincing evidence for this modelling concept.

(4) The numerical model also predicted mesosegregation, i.e. channel segregates (or segregation channels), which qualitatively agrees with the experiment. Similar to many other numerical [6,46] and experimental studies [47], the segregation channels were predicted to occur preferentially near the wall. It must also be stated that the current modelling results can be used only to evaluate the occurrence (or probability/risk of occurrence) of channel segregates. Details of the channel segregates, e.g. the channel quantity and size, are still mesh-size-dependent.

Conflict of interest

The authors declared that there is no conflict of interest.

Acknowledgements

The authors acknowledge the financial support from the Austrian Research Promotion Agency (FFG) through the Bridge Early Stage project (No. 842441), as well as the technical support of industrial partner Primetals (formerly Siemens VAI).

Appendix A. Production of equiaxed crystals by fragmentation

Transport of the number density of the equiaxed crystals, n_{eq}, is described by

$$\frac{\partial}{\partial t} n_{eq} + \nabla \cdot (\vec{u}_e n_{eq}) = N_{frag}, \tag{A.1}$$

where N_{frag} is the source term of equiaxed crystals by fragmentation [49].

It is known that transport of the solute-enriched melt by the interdendritic flow in the columnar-growth direction would lead to remelting [32,50]. Under normal diffusion-governed solidification condition, the driving force for the remelting is the constitutional supersaturation, $(c_\ell - c_\ell^*)$, where c_ℓ and c_ℓ^* are the volume-averaged concentration of interdendritic melt and the thermodynamic equilibrium concentration of the melt at the liquid-solid interface. A positive value of $(c_\ell - c_\ell^*)$ results in remelting, or a process leading to an increase of c_ℓ promotes remelting. The interdendritic melt has usually a concentration gradient (∇c_ℓ) in opposite to the columnar-growth direction for alloys with the solute partition coefficient (k) less than one (Fig. A.1). An interdendritic flow in the columnar-growth direction means $-(\vec{u}_\ell - \vec{u}_c) \cdot \nabla c_\ell > 0$; therefore, the flow leads to local increase of c_ℓ, promoting the remelting. Actually, the rate of remelting should be somehow related to the value of $-(\vec{u}_\ell - \vec{u}_c) \cdot \nabla c_\ell$. Even the local capillary effect, i.e. coarsening or ripening phenomenon, is ignored, fragments can be produced by the 'homogenous' remelting. Based on the large number of experimental facts on the remelting-induced fragmentation [28–30,42,51,52] and the above theoretical analysis, we assume that the rate of fragmentation is proportional to the value of $-(\vec{u}_\ell - \vec{u}_c) \cdot \nabla c_\ell$, by suggesting following formulation for the fragmentation-induced mass transfer rate from the columnar phase to the equiaxed phase:

$$M_{ce} = -\gamma \cdot (\vec{u}_\ell - \vec{u}_c) \cdot \nabla c_\ell \cdot \rho_e. \tag{A.2}$$

The mass integral of all fragments as produced per time, $kg \cdot m^{-3} \cdot s^{-1}$, is proportional to the increase rate of constitutional supersaturation as caused by the interdendritic flow.' Here a fragmentation coefficient' γ is assigned to bridge the unknown correlation between M_{ce} and the increase rate of constitutional supersaturation. In other words, all other unknown contributing factors for the remelting-induced fragmentation such as the curvature effect of the dendrites, latent heat induced thermal fluctuation, diffusion in the interdendritic melt, etc. are included in the single coefficient γ. It must be determined experimentally, or estimated reversely from some available experimental information. As shown in Fig. A.1, we assume that the fragment is globular (spherical) with a diameter proportional to the secondary dendrite arm and the volume fraction of the melt:

$$d^0_{e,frag} = \lambda_2 f_c. \tag{A.3}$$

Hence the rate of the fragment production can be calculated as:

$$N_{frag} = \frac{M_{ce}}{\rho_e \cdot \frac{\pi}{6} \left(d^0_{e,frag}\right)^3} \tag{A.4}$$

Correspondingly, the fragmentation induced momentum transfer $(\vec{U}^p_{ce})$, energy transfer (Q^p_{ce}) and species transfer (C^p_{ce}) from the columnar to equiaxed phases are:

$$\vec{U}^p_{ce} = \vec{u}_c \cdot M_{ce}, \tag{A.5}$$

$$Q^p_{ce} = h_c \cdot M_{ce}, \tag{A.6}$$

$$C^p_{ce} = c_c \cdot M_{ce}, \tag{A.7}$$

with $\vec{u}_c$, h_c, c_c being the moving velocity, the enthalpy and the concentration of the columnar phase. Accordingly, the diameter of equiaxed crystals are shown as

$$d_e = (6 f_e / \pi \cdot n_e)^{1/3}. \tag{A.8}$$

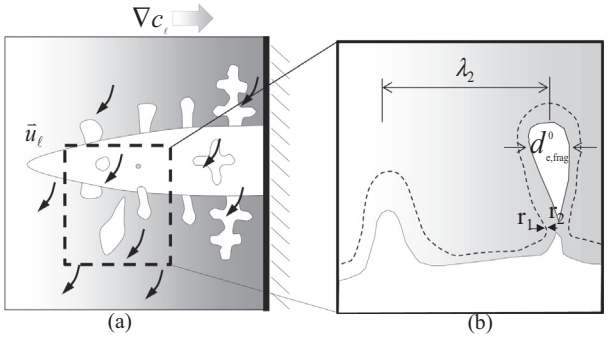

Fig. A.1. Schematic description of remelting-induced fragmentation: (a) transport of solute-enriched interdendritic melt by the flow, and (b) formation of a fragment by remelting of the side arm.

References

[1] D. Hebditch, J. Hunt, Observations of ingot macrosegregation on model systems, Metall. Mater. Trans. 5 (1974) 1557–1564.
[2] C. Gau, R. Viskanta, Melting and solidification of a metal system in a rectangular cavity, Int. J. Heat Mass Transfer 27 (1984) 113–123.
[3] J. Sarazin, A. Hellawell, Channel formation in Pb-Sn, Pb-Sb, and Pb-Sn-Sb alloy ingots and comparison with the system NH_4Cl-H_2O, Metall. Mater. Trans. A 19 (1988) 1861–1871.
[4] M.I. Bergman, D.R. Fearn, J. Bloxham, M.C. Shannon, Convection and channel formation in solidifying Pb-Sn alloys, Metall. Mater. Trans. A 28 (1997) 859–866.
[5] X. Wang, Y. Fautrelle, An investigation of the influence of natural convection on tin solidification using a quasi two-dimensional experimental benchmark, Int. Heat Mass Transfer 52 (2009) 5624–5633.
[6] R. Boussaa, L. Hachani, O. Budenkova, V. Botton, D. Henry, K. Zaidat, H.B. Hadid, Y. Fautrelle, Macrosegregations in Sn-3wt% Pb alloy solidification: experimental and 3D numerical simulation investigations, Int. J. Heat Mass Transfer 100 (2016) 680–690.
[7] L. Hachani, K. Zaidat, Y. Fautrelle, Experimental study of the solidification of Sn-10 wt.%Pb alloy under different forced convection in benchmark experiment, Int. J. Heat Mass Transfer 85 (2015) 438–454.
[8] L. Hachani, B. Saadi, X.D. Wang, A. Nouri, K. Zaidat, A. Belgacem-Bouzida, L. Ayouni-Derouiche, G. Raimondi, Y. Fautrelle, Int. J. Heat Mass Transfer 55 (2012) 1986–1996.
[9] M. Wu, A. Ludwig, A three-phase model for mixed columnar-equiaxed solidification, Metall. Mater. Trans. A 37A (2006) 1613–1631.
[10] C.-A. Gandin, T. Carozzani, H. Digonnet, S. Chen, G. Guillemot, Direct Modeling of structures and segregations Up to industrial casting scales, JOM 65 (2013) 1122–1130.
[11] T. Carozzani, C.-A. Gandin, H. Digonnet, M. Bellet, K. Zaidat, Y. Fautrelle, Direct simulation of a solidification benchmark experiment, Metall. Mater. Trans. A 44 (2013) 873–887.
[12] A. Ciobanas, Y. Fautrelle, Ensemble averaged multiphase Eulerian model for columnar/equiaxed solidification of a binary alloy: I. The mathematical model, J. Phys. D: Appl. Phys. 40 (2007) 3733–3741.
[13] A. Ciobanas, Y. Fautrelle, Ensemble averaged multi-phase Eulerian model for columnar/equiaxed solidification of a binary alloy: II. Simulation of the columnar-to-equiaxed transition (CET), J. Phys. D: Appl. Phys. 40 (2007) 4310–4336.
[14] M. Wu, A. Fjeld, A. Ludwig, Modelling mixed columnar-equiaxed solidification with melt convection and grain sedimentation–Part I: Model description, Comp. Mater. Sci. 50 (2010) 32–42.
[15] M. Wu, A. Ludwig, A. Fjeld, Modelling mixed columnar-equiaxed solidification with melt convection and grain sedimentation–Part II: Illustrative modelling results and parameter studies, Comp. Mater. Sci. 2010 (50) (2010) 43–58.
[16] C. Wang, C. Beckermann, Equiaxed dendritic solidification with convection: Part I. Multiscale/multiphase modeling, Metall. Mater. Trans. A 27 (1996) 2754–2764.
[17] H. Combeau, M. Bellet, Y. Fautrelle, D. Gobin, E. Arquis, O. Budenkova, B. Dussoubs, Y. Du Terrail, A. Kumar, C.-A. Gandin, Analysis of a numerical benchmark for columnar solidification of binary alloys, IOP Conf. Series: Mate. Sci. Eng. 33 (2012) 012086.
[18] M. Wu, A. Ludwig, Using a three-phase deterministic model for the columnar-to-equiaxed transition, Metall. Mater. Trans. A 38A (2007) 1465–1475.
[19] J. Li, M. Wu, A. Ludwig, A. Kharicha, Simulation of macrosegregation in a 2.45-ton steel ingot using a three-phase mixed columnar-equiaxed model, Int. J. Heat Mass Transfer 72 (2014) 668–679.
[20] M. Ahmadein, M. Wu, J. Li, P. Schumacher, A. Ludwig, Prediction of the As-Cast Structure of Al-4.0 Wt Pct Cu Ingots, Metall. Mater. Trans. A 44 (2013) 2895–2903.
[21] J. Li, M. Wu, J. Hao, A. Ludwig, Simulation of channel segregation using a two-phase columnar solidification model–Part I: Model description and verification, Comp. Mater. Sci. 55 (2012) 407–418.
[22] J. Li, M. Wu, J. Hao, A. Kharicha, A. Ludwig, Simulation of channel segregation using a two-phase columnar solidification model–Part II: Mechanism and parameter study, Comp. Mater. Sci. 55 (2012) 419–429.
[23] Y. Zheng, M. Wu, A. Kharicha, A. Ludwig, An attempt to incorporate fragmentation into a volume average solidification model, Model. Simul. Mater. Sci. Eng. 26 (2018) 015004.
[24] J. Hunt, Steady state columnar and equiaxed growth of dendrites and eutectic, Mater. Sci. Eng. 65 (1984) 75–83.
[25] Y. Zheng, M. Wu, A. Kharicha, A. Ludwig, Numerical analysis of macrosegregation in vertically solidified Pb-Sn test castings–Part II: Equiaxed solidification, Comp. Mater. Sci. 124 (2016) 456–470.
[26] A. Ludwig, M. Wu, Modeling of globular equiaxed solidification with a two-phase approach Metall, Mater. Trans. A 33 (2002) 3673–3683.
[27] R.B. Bird, W.E. Stewart, E.N. Lightfoot, Transport Phenomena, Wiley, 2006.
[28] K. Jackson, J. Hunt, D. Uhlmann, T. Seward, On the origin of the equiaxed zone in castings, Trans. Metall. Soc. Aime 236 (1966) 149–158.
[29] W. Montgomery, F. Incropera, Fragmentation of dendritic crystals during solidification of aqueous ammonium chloride, Exp. Heat Transfer 11 (1998) 59–86.
[30] R. Mathiesen, L. Arnberg, P. Bleuet, A. Somogyi, Crystal fragmentation and columnar-to-equiaxed transitions in Al-Cu studied by synchrotron X-ray video microscopy, Metall. Mater. Trans. A 37 (2006) 2515–2524.
[31] E. Liotti, A. Lui, R. Vincent, S. Kumar, Z. Guo, T. Connolley, I. Dolbnya, M. Hart, L. Arnberg, R. Mathiesen, A synchrotron X-ray radiography study of dendrite fragmentation induced by a pulsed electromagnetic field in an Al–15Cu alloy, Acta Mater. 70 (2014) 228–239.
[32] T. Campanella, C. Charbon, M. Rappaz, Grain refinement induced by electromagnetic stirring: a dendrite fragmentation criterion, Metall. Mater. Trans. A 35 (2004) 3201–3210.
[33] M. Bellet, H. Combeau, Y. Fautrelle, D. Gobin, M. Rady, E. Arquis, O. Budenkova, B. Dussoubs, Y. Duterrail, A. Kumar, Call for contributions to a numerical benchmark problem for 2D columnar solidification of binary alloys, Int. J. Therm. Sci. 48 (2009) 2013–2016.
[34] O.L. Rocha, C.A. Siqueira, A. Garcia, Heat flow parameters affecting dendrite spacings during unsteady-state solidification of Sn-Pb and Al-Cu alloys, Metall. Mater. Trans. A 34 (2003) 995–1006.
[35] M. Wu, J. Li, A. Ludwig, A. Kharicha, Modeling diffusion-governed solidification of ternary alloys–Part 1: Coupling solidification kinetics with thermodynamics, Comp. Mater. Sci. 79 (2013) 830–840.
[36] M. Wu, J. Li, A. Ludwig, A. Kharicha, Modeling diffusion-governed solidification of ternary alloys–Part 2: Macroscopic transport phenomena and macrosegregation, Comp. Mater. Sci. 92 (2014) 267–285.
[37] N. Ahmad, J. Rappaz, J.-L. Desbiolles, T. Jalanti, M. Rappaz, H. Combeau, G. Lesoult, C. Stomp, Numerical simulation of macrosegregation: a comparison between finite volume method and finite element method predictions and a confrontation with experiments, Metall. Mater. Trans. A 29 (1998) 617–630.
[38] E. Cadirli, M. Gündüz, The directional solidification of Pb-Sn alloys, J. Mater. Sci. 35 (2000) 3837–3848.
[39] M. Klassen, J. Cahoon, Interdiffusion of Sn and Pb in liquid Pb-Sn alloys, Metall. Mater. Trans. A 31 (2000) 1343–1352.
[40] X.D. Wang, P. Petitpas, C. Garnier, J.-P. Paulin, Y. Fautrelle, A quasi two-dimensional benchmark experiment for the solidification of a tin–lead binary alloy, Comptes Rendus Mécanique 335 (2007) 336–341.
[41] M. Rappaz, Modeling and characterization of grain structures and defects in solidification, Curr. Opin. Solid State Mater. Sci. 20 (2016) 37–45.
[42] A. Hellawell, S. Liu, S. Lu, Dendrite fragmentation and the effects of fluid flow in castings, JOM 49 (1997) 18–20.
[43] C. Wang, S. Ahuja, C. Beckermann, H. De Groh, Multiparticle interfacial drag in equiaxed solidification, Metall. Mater. Trans. B 26 (1995) 111–119.
[44] C. Beckermann, J. Gu, W. Boettinger, Development of a freckle predictor via rayleigh number method for single-crystal nickel-base superalloy castings, Metall. Mater. Trans. A 31 (2000) 2545–2557.
[45] M. Worster, J. Wettlaufer, Natural convection, solute trapping, and channel formation during solidification of saltwater, J. Phys. Chem. B 101 (1997) 6132–6136.
[46] J. Guo, C. Beckermann, Three-dimensional simulation of freckle formation during binary alloy solidification: effect of mesh spacing, Numer. Heat Transfer: Part A: Appl. 44 (2003) 559–576.
[47] D. Ma, Q. Wu, A. Bührig-Polaczek, Some new observations on freckle formation in directionally solidified superalloy components, Metall. Mater. Trans. B 43 (2011) 344–353.
[48] A. Kumar, B. Dussoubs, M. Založnik, H. Combeau, Effect of discretization of permeability term and mesh size on macro-and meso-segregation predictions, J. Phys. D: Appl. Phys. 42 (2009) 105503–105515.
[49] C. Beckermann, Modeling segregation and grain structure development in equiaxed solidification with convection, JOM 49 (1997) 13–17.
[50] M.C. Flemings, G.E. Nereo, Macrosegregation: Part I, Trans. Metall. Soc. Aime 239 (1967) 1449–1462.
[51] M. Christenson, W. Bennon, F. Incropera, Solidification of an aqueous ammonium chloride solution in a rectangular cavity—II. Comparison of predicted and measured results, Int. J. Heat Mass Transfer 32 (1989) 69–79.
[52] M. Christenson, F. Incropera, Solidification of an aqueous ammonium chloride solution in a rectangular cavity—I. Experimental study, Int. J. Heat Mass Transfer 32 (1989) 47–68.